The nanostructure evolution in Fe-C systems under irradiation at 560 K

V. Jansson[a,b,*], M. Chiapetto[a], L. Malerba[a]

[a] *Institute of Nuclear Materials Science, SCK•CEN, Boeretang 200, 2400* Mol, Belgium
[b] *Department of Physics, P.O. Box 43 (Pehr Kalms gata 2), FI-00014* University of Helsinki, Finland

arXiv:1407.7215v1 [cond-mat.mtrl-sci] 27 Jul 2014

Abstract

This work extends our Object Kinetic Monte Carlo model for neutron irradiation-induced nanostructure evolution in Fe-C alloys to consider higher irradiation temperatures. The previous study concentrated on irradiation temperatures < 370 K. Here we study the evolution of vacancy and self-interstitial atom (SIA) cluster populations at the operational temperature of light water reactors, by simulating specific reference irradiation experiments.

Following our previous study, the effect of carbon on radiation defect evolution can be described in terms of formation of immobile complexes with vacancies, that in turn act as traps for SIA clusters. This dynamics is simulated using generic traps for SIA and vacancy clusters. The traps have a binding energy that depends on the size and type of the clusters and is also chosen on the basis of previously performed atomistic studies. The model had to be adapted to account for the existence of two kinds of SIA clusters, $\langle 111 \rangle$ and $\langle 100 \rangle$, as observed in electron microscopy examinations of Fe alloys neutron irradiated at the temperatures of technological interest.

The model, which is fully based on physical considerations and only uses a few parameters for calibration, is found to be capable of reproducing the experimental trends, thereby providing insight into the physical mechanisms of importance to determine the type of nanostructural evolution undergone by the material during irradiation.

Keywords: Fe-C alloys, Object Kinetic Monte Carlo

1. Introduction

The pressurized vessel of nuclear power plant reactors is generally an irreplaceable component, the integrity of which determines the lifetime of the installation. Prolonged exposure to irradiation causes hardening and embrittlement of the steel used to fabricate the vessel, which thereby might lose its capability to maintain integrity in case of an accident. It is therefore important to understand the origin of this hardening and embrittlement. It is known that changes in mechanical properties induced by irradiation can be understood in terms of changes in the micro- or nanostructure of the material.

In this context, iron-carbon (Fe-C) alloys are archetypal model materials for low-alloy ferritic steels, such as those used for reactor pressure vessels of existing light water nuclear reactors. In particular, the generally-agreed mechanistic framework within which RPV steel hardening and embrittlement are understood involves the contribution of three damage components: (i) matrix damage, (ii) precipitates, and (iii) grain boundary de-cohesion due to segregation [1]. It is generally assumed that the first component, dominated by point-defects created in the matrix (iron), can be studied by reference to the behaviour of Fe-C [2].

In this framework, this paper is a continuation of the work to develop a computer model for the nanostructure evolution in iron-carbon (Fe-C) alloys under irradiation, using the Object Kinetic Monte Carlo (OKMC) simulation technique. In our model, we study how the populations of SIA and vacancy clusters evolve over time and increasing damage accumulation in terms of displacements per atom (dpa). The clusters are described in the model by a set of parameters that define their stability, their diffusion properties, and their possibility of interacting with each other and with other defects and the pre-existing microstructure.

In [3, 4] we presented a set of mechanisms and parameters valid for irradiated Fe-C systems at low temper-

*Corresponding author. Tel. +32 1433 3096, fax: +32 1432 1216.
Email address: ville.b.c.jansson@gmail.com (V. Jansson)

ature, below 370 K. At this temperature, transmission electron microscope examinations reveal the formation under neutron irradiation of only prismatic dislocation loops with $1/2\langle 111\rangle$ Burgers vector [5, 6]. The same low temperature Fe-C system has also recently been studied using cluster dynamics modelling [7]. However, at higher temperature a vast majority of loops with $\langle 100\rangle$ loops is observed [5, 8]. The stability and the diffusion properties of $\langle 100\rangle$ loops are significantly different from those of $1/2\langle 111\rangle$ loops [9, 10]. The model must therefore be adapted to take this into account, in order to be applied to higher temperature conditions. We extend here the model to higher temperatures by taking as reference the irradiation experiment from the REVE campaign [5, 8, 11, 12, 13, 14], where the irradiation temperature was 563–568 K. The "pure" Fe material in that experiment is estimated to contain less than 20 wt. ppm C. The average grain size is 250 μm and the dislocation density is reported to be $(7 \pm 2) \cdot 10^{13}$ m^{-2} The irradiation was performed in the in-pile section 2 of the CALLISTO loop of the BR2 reactor in SCK•CEN in Mol, Belgium. The material was irradiated for 16 days until 0.19 dpa had accumulated. The fluence was $\sim 13.1 \cdot 10^{19}$ n cm^{-2}, $E > 1$ MeV [5]. This corresponds to a dpa rate of $1.37 \cdot 10^{-7}$ dpa/s. After irradiation, the material was studied using positron annihilation spectroscopy (PAS) [11, 12, 13, 15], small-angle neutron scattering (SANS) [14] and transmission electron microscopy (TEM) [8]. These different experimental techniques gives a thorough description of the nanostructure of the material in terms of defect densities and average vacancy and SIA cluster sizes.

2. Computation method

We use the LAKIMOCA code for our OKMC simulations [16]. The approach we use is explained in detail in [3] and [4]. For convenience, we highlight here the fundamental ideas on the method.

OKMC is a stochastic simulation technique that considers the migration and interactions of objects in a predefined system with parameterized probabilities. The objects represent in our case vacancy and SIA clusters. Their shapes are usually spherical, except for large SIA clusters, that are represented by toroids. Reactions, such as clustering or annihilation, take place when the objects overlap geometrically. The probability for the objects to perform a migration jump are given in terms of Arrhenius frequencies for thermally activated events,

$$\Gamma_i = \nu_i \exp\left(\frac{-A_i}{k_B T}\right), \tag{1}$$

where ν_i is the attempt frequency of event i, A_i the activation energy, k_B Boltzmann's constant and T the temperature. Events are randomly chosen according to their probability, according to the Monte Carlo algorithm [17]. The simulated time is increased according to the residence time algorithm [18] with

$$\Delta t = \frac{1}{\sum_{i=1}^{N_{int}} \Gamma_i + \sum_{j=1}^{N_{ext}} P_j}, \tag{2}$$

where N_{int} is the number of internal events such as defect jumps and N_{ext} the number of external events, such as cascades or Frenckel pair creation, with P_j being the probabilities for the external events. In the long term, Eq. (2) is indeed equivalent to

$$\Delta t' = -\ln R \Delta t, \tag{3}$$

where R is a uniform random number between 1 and 0 [19].

Traps and sinks are immobile spherical objects that can either trap clusters with a certain binding energy, E_t^δ, that may depend on the size of the trapped cluster, or remove them from the system. In LAKIMOCA, different traps have to be specified for different kinds of defects, such as vacancies and SIA clusters. We use traps to simulate the effect of carbon-vacancy clusters, that are able to trap SIA or vacancy clusters. Sinks are used to simulate the effect of dislocations. SIA clusters are observed by TEM to decorate dislocations [8], meaning they are not absorbed if large enough. We therefore only allow SIA clusters smaller than the core of the dislocations, *i.e.* size 1–4, to be absorbed by the sinks. The number density and radius of the spherical sinks are defined to equal the sink strength of the dislocation density in the material (See [20]). The sink radius, R_s^δ, is thus obtained as

$$R_s^\delta = \frac{\rho V}{4\pi N_s} Z^\delta - r_1^\delta \tag{4}$$

where $\delta = v$ denote parameters for vacancies and $\delta = i$ parameters for SIA. V is the volume of the simulation box, N_s is the number of sinks. The defect radius r^δ has to be removed from the sink radius as the original sink strength expressions were derived for point-like defects. The radius $r_1^v = 4.32 \cdot 10^{-10}$ m is the capture radius of a single vacancy and $r_1^i = 5.17 \cdot 10^{-10}$ m the capture radius for a single SIA. The bias factor takes into account the strain field of defects. Since the strain field of SIA,

compared to vacancies, is larger. $Z^v = 1.0$ and for SIA sinks, we tried different values.

Neutron or ion irradiation is simulated by introducing populations of vacancy and SIA clusters into the system with a certain rate per time and volume, corresponding to a certain dpa rate. The dpa is calculated according to the NRT standard [21, 22]

$$dpa = \frac{0.8E_{MD}}{2E_D}, \tag{5}$$

where E_{MD} is the damage energy, the fraction of the kinetic energy of the primary knock-on atom (PKA) spectrum that is not absorbed by electronic excitation, and is well approximated by the energy of the cascades in the MD simulations. The displacement threshold energy is $E_D = 40$ eV. The cascade cluster populations are chosen randomly from a database with displacement cascade simulations [23, 24, 25, 26, 27, 28]. The MD simulations were performed using the Finnis-Sinclair potential [29] and using energies of 5 keV, 10 keV, 20 keV, 30 keV, 40 keV, 50 keV and 100 keV.

As anticipated in the introduction, in order to extend to higher temperatures the model that we presented in [3] for irradiation temperatures <370 K, it is necessary to allow for the presence of two types of loops. At low irradiation temperatures all SIA clusters could be assumed to be of $1/2\langle 111\rangle$ type, because $\langle 100\rangle$ loops are generally not observed after neutron irradiation in that temperature range [6, 30, 31, 32], with only one exception for ultra-high pure Fe [32], even though $\langle 100\rangle$ loops can be produced under electron irradiation at temperatures as low as 140 K [33].

At higher temperature (550–600 K), however, the fact that $\langle 100\rangle$ loops are always observed obliges the existence of this kind of defect to be somehow considered in the model [5]. The origin of this dominance of $\langle 100\rangle$ SIA clusters above a certain temperature, that depends among other things on the type or irradiation (neutrons or ions), even for a given temperature, is still debated and it is not unambiguously known whether these loops are created in this orientation already in cascades (this is never seen in molecular dynamics simulations of displacement cascades) or they are the result of a subsequent transformation undergone by the clusters produced in the cascade. Here we pragmatically made the implicit assumption that the SIA clusters below the threshold for visibility can be of both kinds, whereas all visible clusters are, by default, of $\langle 100\rangle$ type. This means that the migration energy, M^i, for SIA and the trapping energy, E_t^i, as functions of cluster size, will be different from the parameters used in [3]. Namely, below the visibility threshold, N_{th}, the energy will take an effective value, $M^i = 0.2$ eV (see Sec. 3.3), that corresponds to a hypothetical weighted average between highly mobile $1/2\langle 111\rangle$ loops and slower $\langle 100\rangle$ loops, and similarly the trapping energy will be an effective average value; above the threshold, on the other hand, the value will be the one of $\langle 100\rangle$ loops, $M^i = 0.9$ eV [34]. SIA clusters of sizes between 1 and 5 are considered too small to have Burgers vectors and their migration energy are the same as in [3]. For vacancy clusters, only the trapping energy E_t^v, has been changed, as will be explained later. All other parameters are unchanged and fully described in [3].

Another effect of temperature that must be taken into account is that the carbon-vacancy complexes stable at low and high temperature are not the same (this aspect was already discussed in [3] and applied for the simulation of the post-irradiation annealing). Simulations of small C-V complexes in [3] revealed indeed that the two dominating C-V complexes at temperatures above 450 K are C and C_2V. Molecular dynamics (MD) studies shows that C binds with the edge of a $\langle 100\rangle$-SIA loop with an energy of 1.1 eV, but is repulsed inside the glide prism of the loop. C_2V complexes were calculated to bind to a 61-$\langle 100\rangle$ SIA with an energy of 0.6 eV [35]. As in [3], we simulate the effect of these complexes using generic spherical traps for SIA and vacancies. The estimated amount of C in the the reference material used in the experiment was ~65 appm. If we also include the amount of N atoms, that are assumed to have very similar properties to C atoms, we get a total amount of 134 appm. A priori, other interstitial impurities with similar effects might be present as well, *e.g.* oxygen or hydrogen. Here, and in what follows, they will be formally all confused with C, which is the main one. We then used two kinds of traps for SIA clusters, corresponding to C atoms and C_2V complexes. Since the latter complex contains twice as many C atoms as the former, the total density of traps will be less than the amount of carbon in the system. We used 66 appm of C traps (E_{t1}^v) and 34 appm of C_2V traps (E_{t2}^v); together they correspond to 100 appm and therefore to 134 appm C. The 2:1 ratio of the densities of the two SIA traps were taken from the results of the annealing simulation with carbon explicit in [3]. We used consistently 100 appm of traps for vacancies (E_t^v). The values are listed in Table 1. In this table the only differences with respect to the parameters in [3] concerns clusters above size 6: up to the visibility threshold, migration and trapping energy are effective values that result from an iteration; above the thresh-

old, the trapping energy for ⟨100⟩ loops is taken from [35], while the migration energy was chosen based on indications from work [34] performed using a recently developed on-the-fly KMC scheme [36]. The vacancy trapping energy was also the result of iterations, as is shown in the section on results. The capture radius was 5.0 Å for all traps, as was used in [3, 4].

We used a simulation box size of $450 \times 520 \times 600 a_0^3$, where $a_0 = 2.87 \cdot 10^{-10}$ m is the lattice parameter for α-Fe. Periodic boundary conditions were applied in all three directions. Simulation temperature, grain size, dislocation density, and dpa rate were dictated by the reference experiments in the REVE campaign [11, 12, 13, 14, 8, 15] (See introduction).

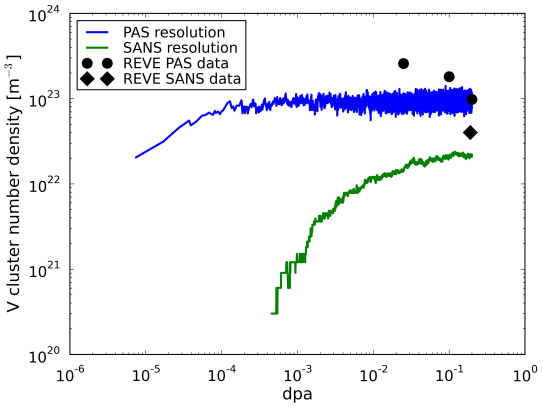

Figure 1: Density of vacancy clusters of sizes observable by PAS and SANS, respectively, versus dpa. The data are compared with PAS [12, 15] and SANS data [14] from the REVE campaign.

3. Results

3.1. The cluster density and mean size evolution compared to the reference experiment

In this section we present the results obtained with the parameter choice that gives globally the best results as compared to experiments. For this we used $N_{th} = 90$, the visibility size threshold for SIA clusters; $E_t^v = 0.2$ eV, the trapping energy of vacancy clusters; and $Z^i = 3.0$, the bias between vacancy and SIA sink radii. The migration energy used is $M^i = 0.2$ eV for SIA clusters of size 6–N_{th} and 0.9 eV above N_{th}. These values will be discussed in more detail in the sections to follow.

The evolution of the vacancy clusters can be compared with results from two different experimental techniques, PAS and SANS, in terms of density and mean cluster size. However, the statistical analysis has to take into account that the two techniques are sensitive to different parts of the vacancy cluster population. PAS is especially suitable for small vacancy clusters, being sensitive even to the presence of single vacancies. However, it provides correct information about the size only for vacancy clusters up to a diameter of ∼1 nm ($N^v \sim 50$), above which all clusters sizes are indistinguishable. SANS, on the other hand, can not detect clusters smaller than ∼1 nm in diameter.

In Fig. 1 the number density of vacancy clusters of all sizes is shown as a function of dose. The density at 0.2 dpa is 10^{23} m^{-3}, which coincides with the experimental PAS value [12, 15]. The vacancy cluster mean size versus dpa is shown in Fig. 2 and the size distribution at 0.2 dpa is shown in Fig. 3. The over-all mean size is ∼2 nm. If one considers that PAS does not distinguish a 50 vacancy cluster from bigger ones, the mean size is ∼0.7 nm, which is only slightly larger than the experimental PAS value of 0.6 nm [12, 15].

If we now consider only the cluster population detectable by SANS, the mean size is ∼3 nm and the density $2.20 \cdot 10^{22}$ m^{-2}. However, in the actual experiment, SANS sees in fact a bimodal size distribution, with one peak at 1.9 nm (cluster diameter) and another one at 8 nm [14]. TEM studies have observed voids with a mean size of 12 ± 0.4 nm and an estimated density of $1.2 \cdot 10^{20}$ m^{-3}. The TEM peak is likely to be the same as the second peak seen by SANS. The density corresponding to this peak with large 8–12 nm clusters is, however, too low to be seen in our simulations. The mean size obtained for clusters larger than 1 nm by the simulations, 3.4 nm, thus corresponds well to the SANS and TEM data, being slightly higher than the main peak value, 1.9 nm, but still between the two peaks. The density of the clusters in the first peak of the SANS distribution is estimated to be $4 \cdot 10^{22}$ m^{-3} [14], slightly above our simulated values.

The best cases for the visible SIA cluster evolution in terms of number density and cluster size are shown in Fig. 4 and Fig. 5, respectively. The density shows good agreement with the experimental data from [8], whereas the mean cluster sizes are a bit underestimated by the model.

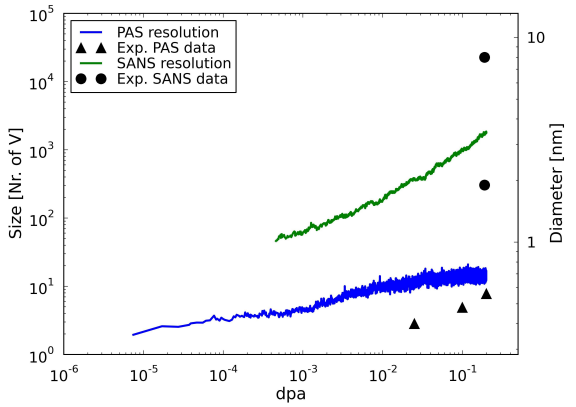

Figure 2: Vacancy cluster mean size versus dpa with PAS and SANS resolution. The experimental PAS data (triangles) are from [12, 15]. The SANS data (bullets) shows the two peaks of the size distribution at 0.2 dpa from [14]. The lower SANS data point is the major peak.

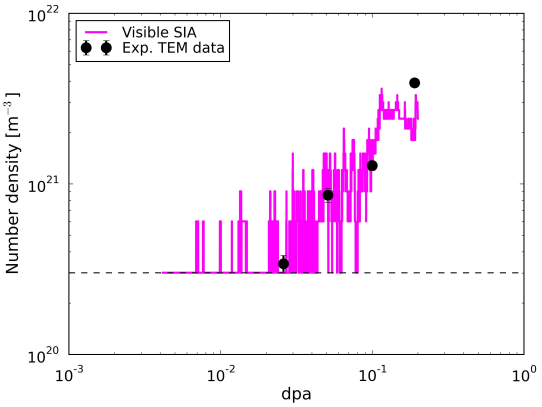

Figure 4: Visible SIA cluster density evolution versus dpa. The experimental TEM data are from [8]. The dotted line correspond to one cluster in the simulated volume.

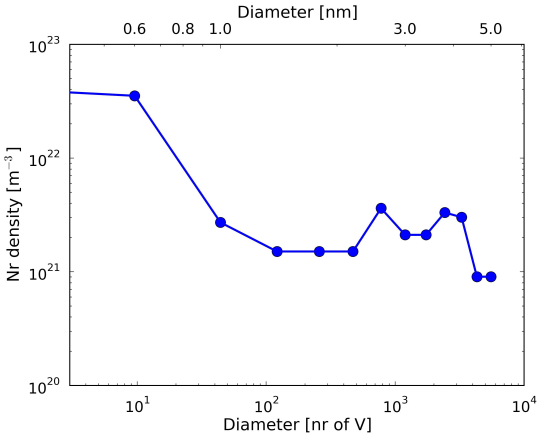

Figure 3: Vacancy cluster size distribution at 0.2 dpa. The bin size is 0.4 nm.

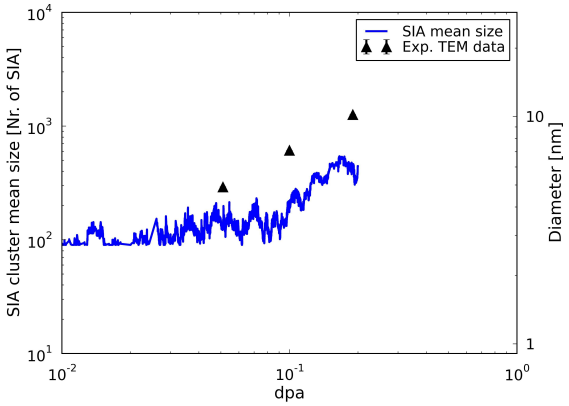

Figure 5: Visible SIA cluster mean cluster size evolution versus dpa. The experimental TEM data are from [8].

Table 1: Overview of the parameters for irradiation temperatures above 370 K, as used in this paper. All are a function of the cluster size, N^δ, where $\delta = i$ for SIA clusters and v for vacancy clusters. M^i is the migration energy for SIA clusters. The values for size 1 to 5 are the same as in [3]. E^i_{t1} and E^i_{t2} are the SIA trapping energies representing C and C_2V complexes, respectively. E^v_t are the trapping energy for vacancy clusters. It is worth noting that the E^i_{t2} energy is only valid up to ~700 K, as the C_2V complexes will dissolve to C atoms and vacancies at this temperature.

N^δ	M^i [eV]	E^i_{t1} [eV]	E^i_{t2} [eV]	E^v_t [eV]
1	0.31	0.17 [37]	0.6	0.65 [37]
2	0.42	0.28 [37]	0.6	1.01 [37]
3	0.42	0.36 [37]	0.6	0.93 [37]
4	0.80	0.34 [37]	0.6	0.96 [37]
5	0.10	0.60 [3]	1.2	1.23 [37]
6	0.20	0.60 [3]	1.2	1.20 [37]
7–N_{th}	0.20	0.60	1.2	0.4
N_{th} <	0.9	1.1	0.6	0.4

3.2. *Effect of the choice of the visibility threshold*

For the SIA migration energy, M^i, for different sizes, as presented in Table 1, there are two values that may change and need to be established: the "effective" migration energy for the "mixture" of ⟨111⟩ and ⟨100⟩ clusters below the threshold for visibility and, to a certain extent, the latter threshold as well. Moreover, the value of 0.9 eV for ⟨100⟩ loops is based only on preliminary calculations. We therefore did trials with different values for M^i below, as discussed in the next section, and above size N_{th} (but above size $N^i > 5$). The values 0.2 eV and 0.9 eV gave the best results. The effect of choosing different threshold sizes for visibility, N_{th}, was also studied. A few cases are shown in Fig. 6 for the visible SIA cluster density. Obviously, a higher N_{th} gives lower visible SIA cluster densities, while the SIA cluster growth seems not to be significantly affected. Using $N_{th} = 90$, good agreement is obtained with the experimental data [8] both in terms of density and mean SIA sizes, the latter being shown for different N_{th} in Fig. 7. No significant impact on the vacancy cluster densities and cluster mean sizes were observed when varying the N_{th} parameter. This is likely because the vacancy trapping energy, E^v_t, which is the important parameter for the vacancy clusters, is not dependent on the N_{th} parameter.

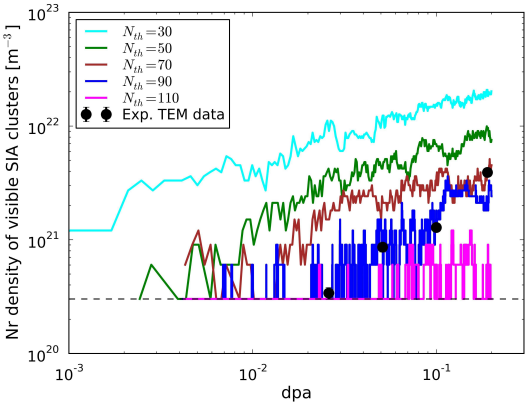

Figure 6: Visible SIA cluster density versus dpa for different values of the visibility threshold, N_{th}. The experimental TEM data are from [8]. The dotted line corresponds to one cluster in the simulated volume.

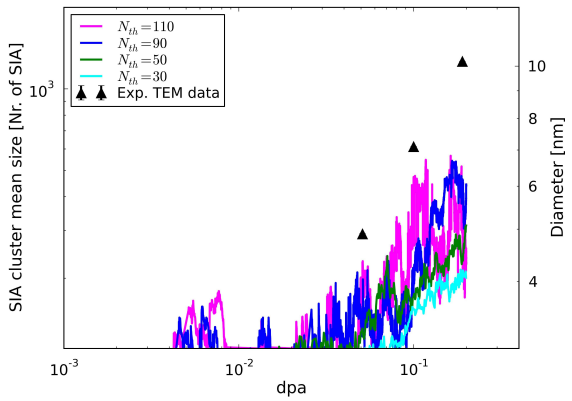

Figure 7: The SIA mean cluster size versus dpa for different values of the threshold, N_{th}. The experimental TEM data are from [8].

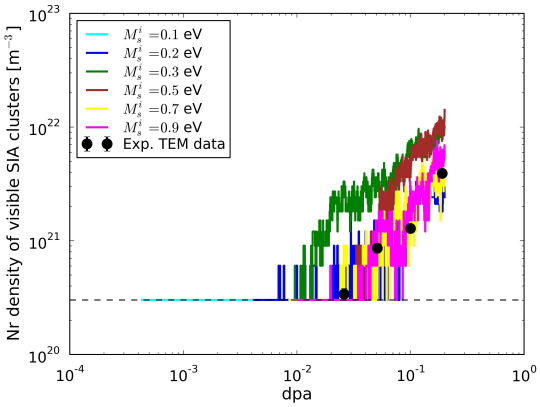

Figure 8: Visible SIA cluster density versus dpa for different migration energies M_s^i for SIA clusters of size $6 \leq N^i < N_{th}$. The experimental TEM data are from [8]. The dotted line corresponds to one cluster in the simulated volume.

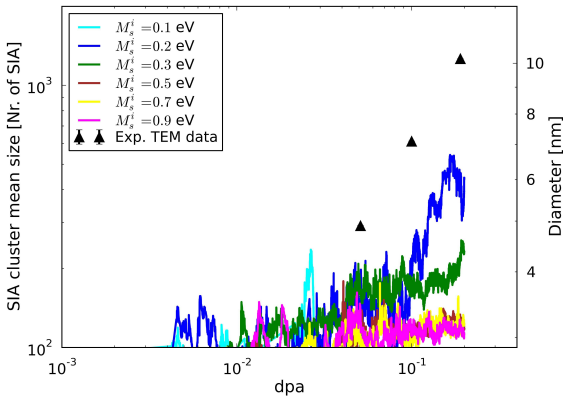

Figure 9: The SIA mean cluster size versus dpa for different migration energies M_s^i for SIA clusters of size $6 \leq N^i < N_{th}$. The experimental TEM data are from [8].

3.3. *Effect of varying the migration energy for invisible SIA clusters*

Figs. 8 and 9 shows the visible SIA cluster density and mean size, respectively, for different migration energy of SIA clusters of small sizes, $6 \leq N^i < N_{th}$, *i.e.* invisible cluster sizes. For sizes above N_{th}, $M^i = 0.9$ eV, as described above and in Table 1. The cluster density does not vary significantly by varying the migration energy between 0.2 eV and 0.9 eV for invisible clusters. With 0.1 eV, no SIA clusters grow above the visibility threshold size, N_{th}. With a slightly higher migration energy, the SIA clusters are slowed down enough for nucleation of larger clusters to occur. Using $M^i = 0.2$ eV, gives the largest mean SIA cluster size and also the best agreement with the experimental data. The effect of the M^i for invisible SIA clusters on the vacancy density and mean cluster size is minimal. Over all, $M^i = 0.2$ eV gives the best result.

3.4. *Effect of varying the vacancy cluster trapping energy*

Vacancies are more mobile at 563 K than at 343 K, which was the irradiation temperature in our previous work [3]. Thus, vacancy traps play a more important role in this situation. In [3], only V clusters of sizes $N^v \leq 6$ were trapped, essentially because precise data were available only up to that size and above it the migration energy was already so large that cluster migration would become a very rare event. In this study we tried different trapping energy for vacancy clusters above size $N^v = 6$. This trapping effect would correspond to the formation of complexes with C or other interstitial impurities. The results are shown in Fig. 10 and 11 for the visible SIA cluster density and mean size evolution, respectively. For the vacancy clusters, the density and mean size evolutions are shown in Fig. 12 and 13 , respectively. It can be seen that this parameter has a quite large effect, when varied. A higher E_t^v increases both the cluster densities and the cluster mean sizes for both SIA and vacancy clusters. The exception to this trend is when considering only the vacancy clusters with the larger SANS resolution, whose mean size actually decreases with increased E_t^v. This effect is likely to be due to the fact that more strongly trapped vacancy clusters lead to a decrease of the number of recombinations and clustering of vacancy clusters, thereby decreasing the mean size of the large vacancy clusters visible by SANS, but increasing both size and density of the smaller vacancy clusters, seen by PAS. Less recombination leads to more SIA clusters and faster SIA cluster growth.

Taking all data for both SIA clusters and vacancies into account, the best fit is given by $E_t^v = 0.4$ eV, because it gives good agreement for the cluster densities and fair agreement for the cluster mean sizes. If higher values are chosen, the mean size is closer to experiment but the density of SIA clusters is totally off, because it builds up and saturates too early. The trapping energy for all vacancy cluster sizes are listed in Table 1. We confirmed by repeating the irradiation experiment at $T = 343$ K,

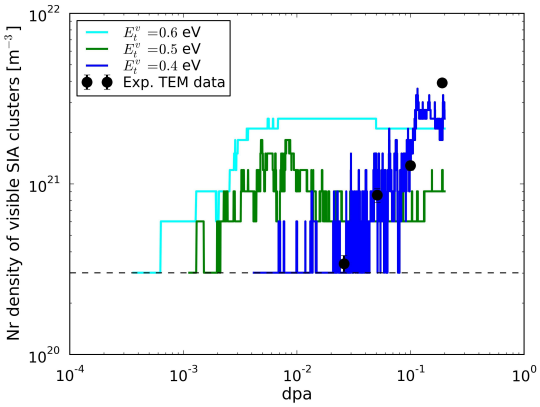

Figure 10: Visible SIA cluster density versus dpa for different values of the trapping energy for vacancy clusters above size 6. The experimental TEM data are from [8]. The dotted line corresponds to one cluster in the simulated system.

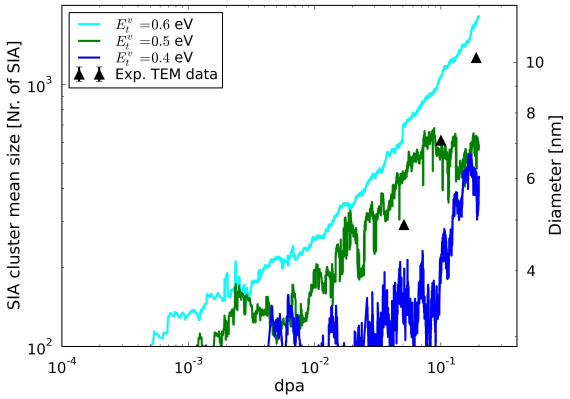

Figure 11: SIA cluster mean size versus dpa for different values of the trapping energy for vacancy clusters above size 6. The experimental TEM data are from [8].

reported in [3], that these E_t^v values do not change the results at lower temperature.

3.5. *Determination of the bias between SIA and vacancy sink radii*

The dislocation density plays a bigger role in this study than in [3, 4], as the density here is larger, $\rho_d = (7 \pm 2) \cdot 10^{13}$ m^{-2}. The effect of changing Z^i is shown in Fig. 14 and 15for what concerns SIA clusters; the effect on the vacancy clusters is shown in Fig. 16 and 17. Somehow, decreasing the value of Z^i has similar effect to increasing the trapping energy for vacancies. A lower Z^i increases the SIA visible cluster density lead to an earlier build up of SIA cluster density and also increases the growth of the SIA clusters. For vacancy clusters, the effect is reversed, so the density and cluster mean size are increased with increased Z^i, even though the effect is more significant for vacancy clusters visible by SANS than at the PAS size resolution. We get good agreement for the cluster density and the vacancy cluster mean size, using $Z^i = 3.0$. For the SIA cluster mean size evolution, the same Z^i underestimates the cluster mean sizes slightly, but remains acceptable. The mean size would be closer to experiment with smaller values of Z^i, but then the density of SIA clusters would be too large and the build up would start too early and with early saturation (Fig. 14).

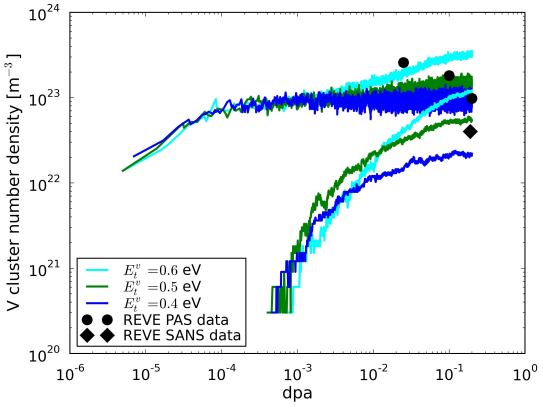

Figure 12: Vacancy cluster densities versus dpa for different E_t^v values. Higher densities are calculated with the PAS size resolution; lower densities with the same colour are calculated with the SANS size resolution. Results are compared with experimental PAS [12, 15] and SANS data [14] from the REVE campaign.

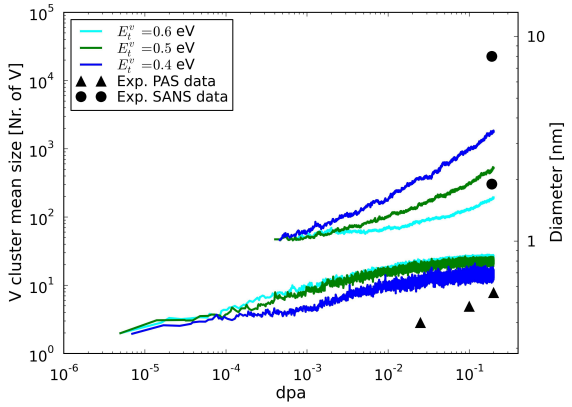

Figure 13: Vacancy cluster mean sizes versus dpa for different E_t^v values. Larger mean sizes are calculated using the SANS size resolution; smaller mean sizes are calculated using the PAS resolution. Results are compared with experimental PAS [12, 15] and SANS data [14] from the REVE campaign. SANS points corresponds to the two peaks in the observed size distribution: the lower point is the major peak.

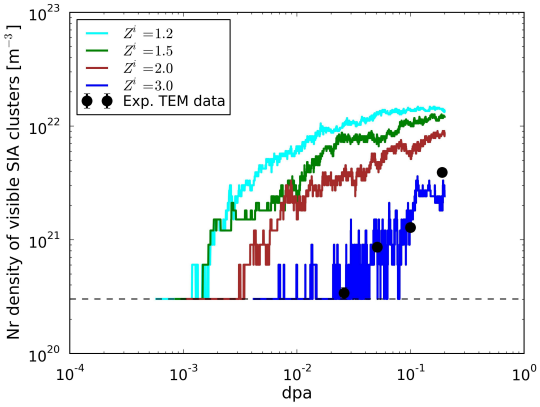

Figure 14: Visible SIA cluster density versus dpa for two different values of the SIA bias factor for sinks, Z^i. The experimental TEM data are from [8]. The dotted line corresponds to one cluster in the simulated volume.

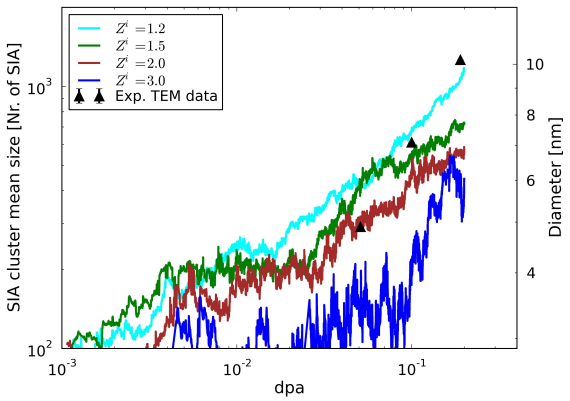

Figure 15: SIA mean cluster size versus dpa. The experimental TEM data are from [8].

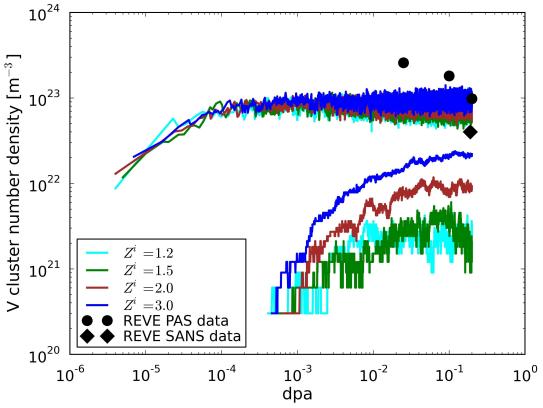

Figure 16: Vacancy cluster densities versus dpa for different Z^i values. The higher densities are calculated with the PAS size resolution, whereas the lower densities with the same colour are calculated with the SANS size resolution. The data are compared with experimental PAS [12, 15] and SANS data [14] from the REVE campaign.

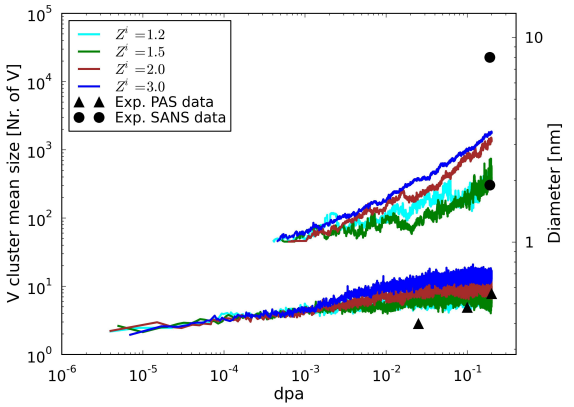

Figure 17: Vacancy cluster mean sizes versus dpa for different Z^i values. Larger mean sizes are calculated using the SANS size resolution; smaller mean sizes are calculated using the PAS resolution. Results are compared with experimental PAS [12, 15] and SANS data [14] from the REVE campaign. SANS points corresponds to the two peaks in the observed size distribution: the lower point is the major peak.

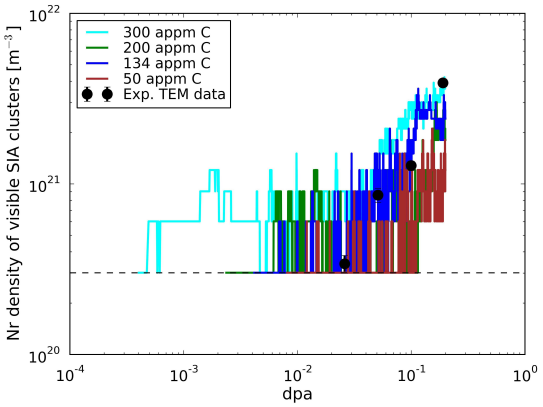

Figure 18: Visible SIA cluster density versus dpa for different C concentrations. The experimental TEM data are from [8]. The dotted line corresponds to one cluster in the simulated system.

3.6. Impact of the concentration of carbon in the matrix

The impact of the C concentration was studied by trying different trap concentrations, as shown in Fig. 18. Our reference experimental material is estimated to have a carbon concentration of 134 appm. Higher trap concentration gives a higher SIA cluster density, but even 200 appm of carbon still gives a fair agreement with the experimental data. Higher C concentrations also increase the mean SIA cluster sizes, as seen in Fig. 19.

The vacancy density increases slightly with increased C concentration from $8.6 \cdot 10^{22}$ m^{-3} (at 0.2 dpa) with 50 appm C to $2.09 \cdot 10^{23}$ m^{-3} with 300 appm C (*Cf.* Fig. 20). If only considering the cluster sizes observable by SANS, these densities increases as well slightly from $1.5 \cdot 10^{22}$ m^{-3} (at 0.2 dpa) with 50 appm to $2.7 \cdot 10^{22}$ m^{-3} with 300 appm C (*Cf.* 21). The experimental SANS value at 0.2 dpa with 134 appm C is $4.0 \cdot 10^{22}$ m^{-3}, so a higher density of C concentration slightly improves the agreement with the experimental SANS data. The density and mean size evolutions are all very similar, with early saturations for all four C concentrations.

The average vacancy cluster size for clusters visible by PAS are very similar for the four different C concentrations; between 0.61 and 0.67 nm and thus in good agreement with the experimental PAS value, 0.6 nm. No clear trend can be observed. For clusters visible by SANS, the mean sizes at 0.2 dpa goes from 4.23 nm with 50 appm C to 2.83 nm with 300 appm C. A larger C density appears to lead to more nucleation and less recombination of vacancy clusters, which leads to higher vacancy cluster densities, but slower growth and thus smaller mean size in the SANS size category, at the dose considered here. Less recombinations also promotes the growth of SIA clusters. The main peak in the SANS bimodal distribution is at a size of 1.9 nm. The agreement of the mean cluster sizes with SANS data thus improves with higher concentration of C, suggesting that the actual content of interstitial impurities in the material might have been higher than reported. It is also quite possible that we have underestimated the number of free C atoms, compared to the number of C_2V complexes. As C atoms are stronger traps than the C_2V complexes, less of the latter complexes gives more nucleation points.

4. Discussion

The evolution of the vacancy and SIA clusters under irradiation are highly dependent on each other, making it delicate to fine-tune parameters of physical significance but unknown value to satisfy the experimental data for both kinds of defects. Changing parameters for vacancies, such as the trapping energy for vacancy clusters, E_t^v, will have a significant effect on the SIA cluster evolution, as we have shown above. For the final set of parameters of our model, we had to fine-tune three parameters: the migration energy of invisible SIA clus-

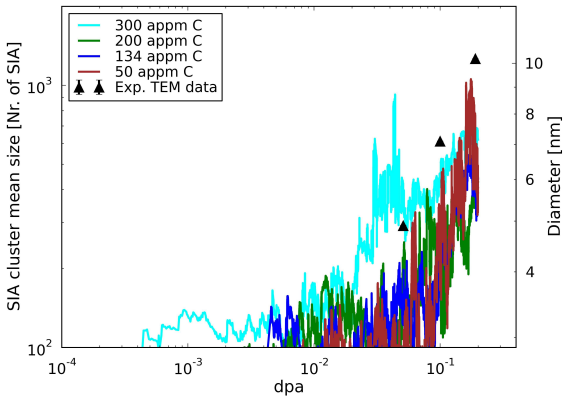

Figure 19: Visible SIA cluster mean size versus dpa for different C concentrations. The experimental TEM data are from [8].

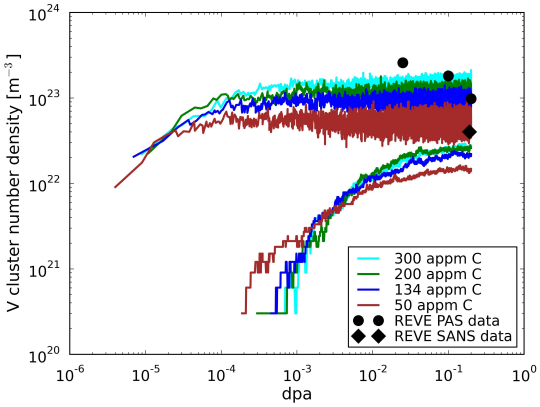

Figure 20: Vacancy cluster densities versus dpa for different C content. The higher densities are calculated with the PAS size resolution, whereas the lower densities with the same colour are calculated with the SANS size resolution. The data are compared with experimental PAS [12, 15] and SANS data [14] from the REVE campaign.

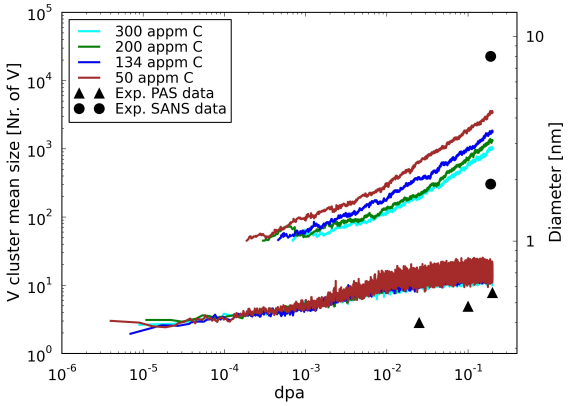

Figure 21: Vacancy cluster mean sizes versus dpa for different C content. Larger mean sizes are calculated using the SANS size resolution; smaller mean sizes are calculated using the PAS resolution. Results are compared with experimental PAS [12, 15] and SANS data [14] from the REVE campaign. SANS points corresponds to the two peaks in the observed size distribution: the lower point is the major peak.

ters, M^i, ($N < N_{th}$), the energy to trap vacancy clusters at impurity atoms or other features, E_t^v and the bias factor, Z^i. The chosen values had to make sense physically and make the simulations satisfy all the experimental data. In the fine-tuning process, it was seen that it is not straightforward to get at the same time good agreement for density and size. A compromise had to be found as, especially in the case of SIA clusters, values of the parameters that improve the mean size significantly increase the density, leading to too early build up and saturation. Although these differences are partially compensated by assuming that the content of interstitial species is higher than the nominal one, quite obviously the model has inherent limitations that we shall discuss in what follows.

One strong limitation is given by the fact that we consider in the model, for the sake of simplicity, a single population of loops, with different features depending on size. These features correspond to either the properties of $\langle 100 \rangle$ loops, of to the properties of a "mixture" of $\langle 100 \rangle$ and $1/2\langle 111 \rangle$ loops. We do not know the proportions of $\langle 100 \rangle$ and $1/2\langle 111 \rangle$-SIA clusters, nor how the former clusters are created. Are they the result of the interaction between $1/2\langle 111 \rangle$ loops created in cascades, as predicted by interatomic potentials [23, 24, 25, 26, 27, 28, 38, 39]? Or do they appear as the result of spontaneous transformation from $1/2\langle 111 \rangle$

loops [33]? Or is there an influence of temperature on their stability that makes them produced directly in cascades, this effect being unknown to the interatomic potentials [9]? Discussing the plausibility of these possibilities goes beyond the scope of the present work. Given this uncertainty, pragmatically we assumed that the type of loop is determined by size: visible loops are $\langle 100 \rangle$, invisible ones are of unknown nature. For these, we make use of an effective value of migration energy $M^i = 0.2$ eV for $6 \leq N^i \leq N_{th}$, where N_{th} is the threshold for visibility. Clearly, a fully physical model should include a proper description of both classes of loops. However, given the uncertainties hinted at above, the development of such a model would imply exploring one by one all possible mechanisms, with the use, unavoidably, of other equally uncertain assumptions. Before such a model can be reliably developed more insight into the physics of SIA clusters is needed, otherwise the increased complexity would not be necessarily rewarded by an increased reliability.

Another strong approximation in our model concerns the fact that we introduce traps that are conceptually associated with the presence of C and C-vacancy complexes trapping SIA clusters, as well as vacancy clusters, but the behaviour of which is only remotely connected with C atoms and the complexes that it forms with defects. To start with, the traps are introduced since the very beginning, while in reality they will first need to form. Secondly, the traps are rigorously immobile and unchanged in nature throughout the simulation, while C atoms are highly mobile at the temperature considered here: the stability of C-vacancy complexes is such that they might be continuously forming and dissociating, and it cannot be excluded that some mechanism of migration of these complexes might exist. The dynamic formation and disappearance of complexes is likely to affect the kinetics of the nanostructural evolution under irradiation and we should probably suppose that the traps we use are somehow more efficient than the actual traps would be. However, again, the removal of this simplifying assumption and the introduction of a complete description of the physics of the traps implies the knowledge of a large number of parameters and mechanisms that we currently know very poorly. So, a more complete model should also eventually make use of assumptions, while being much more complex, thereby making it questionable whether the increased level of physical detail would be rewarded by higher reliability. For the parameterization of the traps, we use *ab initio* values for the interaction of single C atoms with SIA clusters, E^i_{t1}, for sizes up to $N^i = 4$, and also with vacancy clusters, E^v_t, up to size 6 (*Cf.* Table 1). Above these sizes the trapping energies were assumed, guessed or fitted. For the SIA traps, two populations of traps were used, representing the two dominating complexes that are able to trap SIA clusters: C and C_2V. Below size N_{th}, we can assume that the more mobile $1/2\langle 111 \rangle$-SIA clusters, assumed to be present in the "mixture", are more affected by the traps than the slowly moving $\langle 100 \rangle$ clusters, so the trapping energies are chosen to represent the interaction between the former SIA clusters and the C (E^i_{t1}) and C_2V (E^i_{t2}) complexes, respectively. A C atom binds to a $1/2\langle 111 \rangle$-SIA cluster with ~0.6 eV [40]. This value is thus used for E^i_{t1} for $5 \leq N^i \leq N_{th}$. Above size N_{th}, the interaction is assumed to be exclusively with $\langle 100 \rangle$ and we used the MD result for the binding energy between said cluster and the C atom, $E^i_{t1} = 1.1$ eV [35].

The second kind of SIA trap is supposed to represent C_2V complexes. We do not know the exact values for the binding between these complexes and small SIA clusters. We used for the smallest sizes (1–4) $E^i_{t2} = 0.6$ eV. For $N^i \geq 5$, but $< N_{th}$, we fitted the trapping energy to be $E^i_{t2} = 1.2$ eV, which can be seen as an intermediate value between the binding energy between a C_2V cluster and a $1/2\langle 111 \rangle$-SIA cluster, 1.5 eV, or a $\langle 100 \rangle$-SIA cluster, 0.6 eV. We assume SIA clusters larger than N_{th} to be of $\langle 100 \rangle$ type, and $E^i_{t2} = 0.6$ eV corresponds to the binding energy between C_2V complexes and these clusters [35].

For the simulations at lower temperature, 343 K, reported in [3, 4], no trapping of vacancies above size 6 was used. In this study at 563 K, we found that a trapping energy of $E^v_t = 0.4$ eV is necessary. The higher mobility of vacancy clusters at the higher temperature makes the traps more important. At low temperature, the vacancy clusters are so slowly moving that traps have no effect. The vacancy traps represent C and C_2V complexes, even though we assume them both to have the same trapping energies for vacancies. We do not have any knowledge of calculations of the binding energy between vacancy clusters above size 6 and C atoms, making fitting the only option.

The bias factor for SIA sinks, Z^i, as defined in Eq. (4), proved to be an important parameter in our model. The bias factor takes into account the larger strain fields of SIA clusters, as compared to vacancy clusters. In rate theory calculations, the value chosen has usually been between 1.3 and 1.5. However, in order to lower the SIA density and still keep the general trend according to the experimental data, we found that a much higher value of $Z^i = 3.0$ was needed.

It is hard to find a physical explanation for why such a high value is needed and perhaps it is merely a result of other approximations of the model. Possibly, the assumption of immobile traps is responsible here. Indeed, it is as if the C atoms, represented by traps, were immobile in our model. It is possible that several mobile C atoms could attach to the same vacancy or SIA cluster, thereby reducing the number of nucleation points for cluster growth. In our model, the number of traps is constant and given by the nominal C content in the material used in the experiment. We might thus be overestimating the number of nucleation points and, by increasing the sink strength for the SIA sinks by a large value of Z^i, we slow down the nucleation and clustering process at low dpa values. At higher dpa, the clusters are more dominating than the pre-existing sinks and new SIA defects are more likely to contribute to the cluster growth than to disappearing at the sinks. The main effect of a high Z^i is thus a delay of the visible SIA cluster growth. It can be likewise used to explore the effect of different dose rates or high fluence. These studies will be the subject of forthcoming papers.

5. Summary and conclusions

We have developed a physical model that describes nanostructural evolution under irradiation in Fe-C alloys versus dose, at temperatures in the range of the operation conditions of reactor pressure vessel steels. The model reproduces fairly well experimental data, using only a few calibration parameters of clear physical meaning. The main assumptions of the model, based on a combination of experimental and theoretical results, are:

- C atoms and complexes involving C atoms and vacancies, mainly C_2V, act as traps for SIA clusters and their effect can be described in first approximation as immobile traps to which a given trapping energy is associated that depends on the size of the trapped cluster.
- While visible SIA loops have $\langle 100 \rangle$ Burgers vector, those invisible to the electronic microscope include loops of both $\langle 100 \rangle$ and $1/2\langle 111 \rangle$ type, and this fact can be taken into account by using effective migration parameters for invisible clusters.

This model can be used as a starting point to add, explicitly or effectively, the effect of substitutional solute atoms found in reactor pressure vessel steels and known to be responsible for their hardening and embrittlement, such as Cu, Ni and Mn.

Acknowledgement

This work was carried out as part of the PERFORM60 project of the 7th Euratom Framework Programme, partially supported by the European Commission, Grant agreement number FP7-232612.

References

[1] G. R. Odette, G. E. Lucas, Radiation effects and defects in solids 144 (1998) 189–231.
[2] J. T. Buswell, W. Phythian, R. J. McElroy, S. Dumbill, P. H. N. Ray, J. Mace, R. N. Sinclair, Journal of Nuclear Materials 225 (1995) 196–214.
[3] V. Jansson, L. Malerba, Journal of Nuclear Materials 443 (2013) 274–285.
[4] V. Jansson, L. Malerba, Journal of Nuclear Materials 452 (2014) 118–124.
[5] L. Malerba, Experimental reference cases for model validation in Fe and FeC alloys, Technical Report, Public Deliverable Nr. D1–3.10, FP7/Perform60 Collaborative Project, Grant Agreement Nr. FP7-232612, 2011.
[6] S. J. Zinkle, B. N. Singh, Journal of Nuclear Materials 351 (2006) 269–284.
[7] Y. Abe, T. Tsuru, S. Jitsukawa, MRS Online Proceedings Library 1535 (2013) mmm2012–a.
[8] M. Hernández-Mayoral, D. Gómez-Briceño, Journal of Nuclear Materials 399 (2010) 146–153.
[9] S. L. Dudarev, R. Bullough, P. M. Derlet, Physical Review Letters 100 (2008) 135503.
[10] K. Arakawa, K. Ono, M. Isshiki, K. Mimura, M. Uchikoshi, H. Mori, Science 318 (2007) 956.
[11] M. Lambrecht, L. Malerba, A. Almazouzi, Journal of Nuclear Materials 378 (2008) 282–290.
[12] M. Lambrecht, Ph.D. thesis, University of Ghent, 2009.
[13] M. Lambrecht, A. Almazouzi, Journal of Nuclear Materials 385 (2009) 334–338.
[14] F. Bergner, M. Lambrecht, A. Ulbricht, A. Almazouzi, Journal of Nuclear Materials 399 (2010) 129–136.
[15] E. Meslin, M. Lambrecht, M. Hernández-Mayoral, F. Bergner, L. Malerba, P. Pareige, B. Radiguet, A. Barbu, D. Gómez-Briceño, A. Ulbricht, et al., Journal of Nuclear Materials 406 (2010) 73–83.
[16] C. Domain, C. S. Becquart, L. Malerba, Journal of Nuclear Materials 335 (2004) 121–145.
[17] N. Metropolis, A. Rosenbluth, M. N. Rosenbluth, A. H. Teller, E. Teller, The journal of chemical physics 21 (1953) 1087.
[18] W. M. Young, E. W. Elcock, Proceedings of the Physical Society 89 (1966) 735.
[19] A. B. Bortz, M. H. Kalos, J. L. Lebowitz, Journal of Computational Physics 17 (1975) 10–18.
[20] F. A. Nichols, Journal of Nuclear Materials 75 (1978) 32–41.
[21] C. Domain, C. S. Becquart, L. Malerba, in: N. M. Ghoniem (Ed.), Proceedings of Second International Conference on Multiscale Materials Modeling: October 11 - 15, 2004, Los Angeles, California, Mechanical and Aerospace Engineering Department, University of Calif., 2004.

[22] M. T. Norgett, et al., Nuclear Engineering and Design 33 (1975) 50–54.
[23] R. E. Stoller, Journal of Nuclear Materials 233 (1996) 999–1003.
[24] R. E. Stoller, G. R. Odette, B. D. Wirth, Journal of Nuclear Materials 251 (1997) 49–60.
[25] R. E. Stoller, A. F. Calder, Journal of Nuclear Materials 283 (2000) 746–752.
[26] R. E. Stoller, Nuclear Engineering and Design 195 (2000) 129–136.
[27] R. E. Stoller, S. G. Guiriec, Journal of Nuclear Materials 329 (2004) 1238–1242.
[28] R. E. Stoller, Journal of Nuclear Materials 276 (2000) 22–32.
[29] M. W. Finnis, J. E. Sinclair, Philosophical Magazine A 50 (1984) 45–55.
[30] B. L. Eyre, Philosophical Magazine 7 (1962) 2107–2113.
[31] B. L. Eyre, A. F. Bartlett, Philosophical Magazine 12 (1965) 261–272.
[32] I. M. Robertson, M. L. Jenkins, C. A. English, Journal of Nuclear Materials 108 (1982) 209–221.
[33] K. Arakawa, M. Hatanaka, E. Kuramoto, K. Ono, H. Mori, Physical Review Letters 96 (2006) 125506.
[34] Y. N. Osetsky, Private communication, 2013.
[35] N. Anento, A. Serra, Private communication, 2013.
[36] H. Xu, Y. N. Osetsky, R. E. Stoller, Physical Review B 84 (2011) 132103.
[37] C. S. Becquart, C. Domain, PERFORM60 report, 2011.
[38] J. Marian, B. D. Wirth, J. M. Perlado, Physical Review Letters 88 (2002) 255507.
[39] D. A. Terentyev, Study of radiation effects in FeCr alloys for fusion applications using computer simulations, Ph.D. thesis, Université Libre de Bruxelles, 2006.
[40] D. Terentyev, N. Anento, A. Serra, V. Jansson, H. Khater, G. Bonny, Journal of Nuclear Materials 408 (2011) 271–284.